Renewable Energy 83 (2015) 234–244

Contents lists available at ScienceDirect

Renewable Energy

journal homepage: www.elsevier.com/locate/renene

Real-time prediction intervals for intra-hour DNI forecasts

Yinghao Chu, Mengying Li, Hugo T.C. Pedro, Carlos F.M. Coimbra*

Department of Mechanical and Aerospace Engineering, Jacobs School of Engineering, Center of Excellence in Renewable Resource Integration and Center for Energy Research, University of California, 9500 Gilman Drive, La Jolla, CA 92093, USA

ARTICLE INFO

Article history:
Received 23 January 2015
Accepted 8 April 2015
Available online 14 May 2015

Keywords:
Solar forecasting
Prediction intervals
Sky imaging
Support vector machines
Artificial neural networks

ABSTRACT

We develop a hybrid, real-time solar forecasting computational model to construct prediction intervals (PIs) of one-minute averaged direct normal irradiance for four intra-hour forecasting horizons: five, ten, fifteen, and 20 min. This hybrid model, which integrates sky imaging techniques, support vector machine and artificial neural network sub-models, is developed using one year of co-located, high-quality irradiance and sky image recording in Folsom, California. We validate the proposed model using six-month of measured irradiance and sky image data, and apply it to construct operational PI forecasts in real-time at the same observatory. In the real-time scenario, the hybrid model significantly outperforms the reference persistence model and provides high performance PIs regardless of forecast horizon and weather condition.

1. Introduction

Solar energy technologies are both functionally ready and nearly financially competitive to be deployed at large scales to produce clean and renewable power. However, the increasing levels of solar penetration into the power grid and the associated variable nature of solar irradiance caused by atmospheric processes impose challenges to grid management [1,2]. Solar forecasting is an enabling technology to mitigate the instabilities associated with the variability of solar power generation [1,3–5].

There has been strong research interest in developing effective solar forecasting methodologies for the various temporal horizons of interest to solar integration. Most of these models are based on statistical (data-driven) methods [6–20] or physical methods based on either remote sensing or local sensing [3,18,19,21–26]. Hybrid forecasting models that make use of the advantages of both stochastic learning and physical models have been developed in the recent years [18,19,27,28].

All of the above models produce point or time-average forecasts without projecting the uncertainty intervals of the predictions. In practice, there are inherent and irreducible forecasting errors associated with deterministic point forecasts regardless of the data processing, the mechanism of model, the explanatory variables, and the model training methods [29–31]:

$$T(t) = f(t) + \varepsilon(t), \tag{1}$$

where $T(t)$ is the measured (target) value at time t, $f(t)$ is the true regression, and $\varepsilon(t)$ is the unbiased noise. Prediction intervals (PIs), in which target values T will fall with a probability, quantify the uncertainty of forecasts, and therefore are more useful than point predictions for decision-making in real-world applications [29,30,32,33].

Therefore in this work, we develop a smart forecasting model (denoted as the Hybrid model) to provide intra-hour PIs for one-minute averaged Direct Normal Irradiance (DNI), which is the energy source for concentrated solar power technologies and is highly variable due to the direct influence of cloud cover [27]. The Hybrid model integrates Support Vector Machine (SVM) method and Artificial Neural Networks (ANNs) method. The inputs to this Hybrid model are lagged time series of numerical local-sensing information, DNI, and diffuse irradiance (DIF). The Hybrid model first uses the SVM to classify the time series of DNI into two categories: low DNI variability period (lv) and high DNI variability period (hv). Then PIs are generated by ANN_{lv} or ANN_{hv} which are trained with data collected in lv and hv periods, respectively. The prediction horizons of PIs are 5, 10, 15, and 20 min. The Hybrid model is validated in terms of common statistical metrics as well as three performance metrics: PI coverage probability (PICP), PI

* Corresponding author.
E-mail address: ccoimbra@ucsd.edu (C.F.M. Coimbra).

http://dx.doi.org/10.1016/j.renene.2015.04.022
0960-1481/

normalized average width (PINAW), and coverage width-based criterion (CWC) (explained in Section 3.7). The validation performance of Hybrid model is compared with the performance of two reference models: a persistence model and a Bootstrap-ANN model. After the validation, the Hybrid model and the persistence model have been mounted on a CPU server at UCSD and have been producing real-time PI forecasts since July 1st, 2014.

In this paper: the preparation of data used in the Hybrid model development is presented in Section 2. The detailed methods used to create the Hybrid model and the two reference models are presented in Section 3, in which the performance metrics used to assess the accuracy of PIs are also discussed. The results are presented in Section 4 and conclusions are presented in Section 5.

2. Data

DNI and DIF data are collected using a Rotating Shadowband Radiometer (Augustyn RSR-2, Manufactured by Irradiance, Inc) installed in Folsom, California (latitude = 38.6429°N, longitude = 121.1487°W). The RSR-2 simultaneously measures the DNI and DIF components of broadband solar irradiance every 30 s, and a Campbell Scientific CR1000 data logger is used to log the irradiance values. 8-bit RGB sky images (1536 × 1536 pixels) are collected every minute using a generic off-the-shelf, high-resolution fisheye dome network camera installed next to the RSR-2s. This fish-eye camera uses a 3.1 MP CMOS sensor and a 360° panoramic view lens. The captured sky images (see sample images in Fig. 1) are transferred via FTP to a the UCSD server every minute. The irradiance data and the sky images are stored in a MySQL database and are paired as data points.

One year (January 13, 2013 to Dec 31, 2013) of historical data are assigned as a training set for model training. Six months (January 1, 2014 to June 11, 2014) of historical data are assigned as a validation set for model validation. Both the training and validation sets include the possible range of irradiance variability caused by diverse weather conditions. After the model training and validation process (discussed in Section 3), we launched the model in realtime to forecast intra-hour DNI for Folsom. The launched forecasts have been operating every five minutes as unattended task since July 1st, 2014 using live stream of paired irradiance and sky image data from the Folsom observatory.

Data quality is essential for the robustness and accuracy of the forecasts. The RSR-2 is a first-class radiometer that meets the accuracy requirements of this study. The fisheye lens is regularly cleaned to maintain the quality of sky images, and sky images with excessive amount of dust are manually removed from the database. For low sun elevation time, ground obstacles (e.g. trees) adversely affect the accuracy of irradiance measurements. Therefore, the forecasts introduced in this work only consider data points collected during the period when the solar elevation angle is higher than 15°.

3. Methods

In this section we first discuss the image processing method that extracts numerical information of cloud cover (as the inputs to the employed forecasting models). Then we discuss the ANN method, the SVM method, and key steps to generate PIs for the persistence model, the Bootstrap-ANN model, and the Hybrid model. The metrics used to assess the performance of all models are discussed at the end of this section.

3.1. Image processing and numerical inputs

Cloud cover directly affects the magnitude of DNI at the ground level. Therefore, sky images that provide information of cloud cover are useful to the solar forecasts [34]. For a 8-bit RGB sky images, cloud pixels generally have a higher red (R) intensity values than sky pixels. Therefore, the ratio (RBR = R/B), difference (RBD = R − B), or normalized ratio (nRBR=(R − B)/(R + B)) of red intensity to blue intensity are widely used to identify the presence of clouds from images.

Comparing to the RBR and RBD, nRBR shows improved robustness because it avoids extremely large RBRs when pixels have very low blue intensities [26,35]. Examples of original and nRBR images are shown in Fig. 1. Therefore, we use the nRBR parameter to

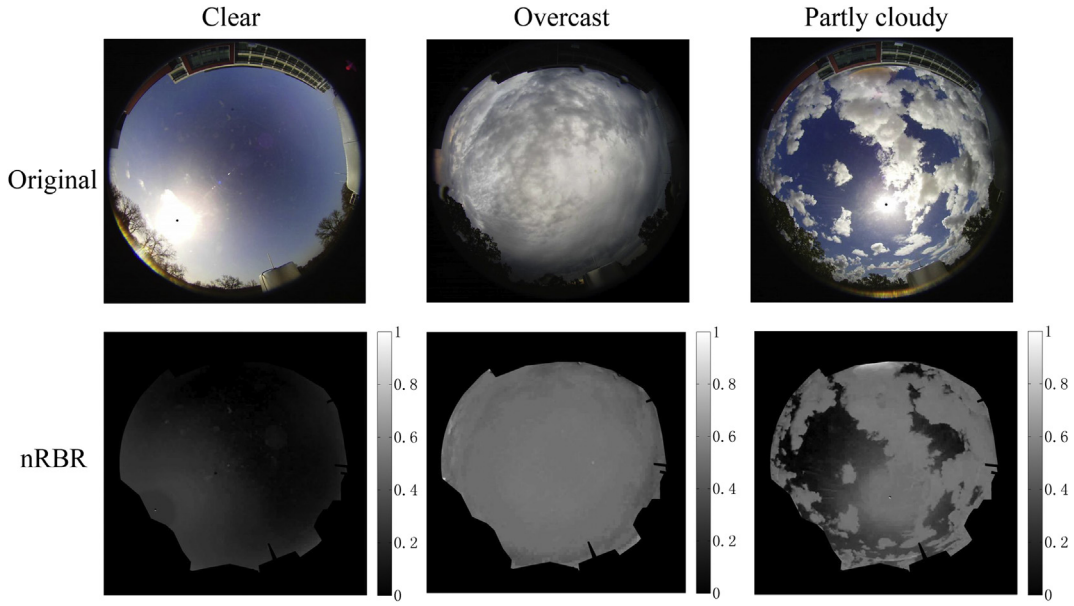

Fig. 1. Examples of original images (top row) and normalized RBR (nRBR) images (bottom row) for clear period (left column), overcast period (mid column), and partly cloudy (right column) period. The greyscales indicate the nRBR magnitudes in each image.

calculate three numerical cloud cover information for a sky image: mean, standard deviation and entropy.

Mean

$$\mu = \frac{1}{N}\sum_{i=1}^{N} \mathrm{nRBR}_i, \tag{2}$$

where N is the number of pixels. Standard deviation

$$\sigma = \sqrt{\frac{1}{N}\sum_{i=1}^{N} (\mathrm{nRBR}_i - \mu)^2}. \tag{3}$$

Entropy

$$e = -\sum_{j=1}^{N_B} p_j log_2\left(p_j\right), \tag{4}$$

where p_j is the relative frequency for the jth bin (out of $N_B = 256$ bins evenly spaced). These three metrics are used as inputs to the proposed forecasting models.

We directly use nRBR without employing cloud detection (detect the actual cloud cover from an image) for two reasons: 1) Cloud detection methods usually require significant amount of processing time which may significantly increase the latency of the real time forecasting. 2) Most of the cloud detection methods available in literature [26,35–41] detect clouds using RBR or nRBR information. Therefore, nRBR-based metrics already represent the cloud cover information and can be directly used to forecast DNI through statistical methods (such as ANNs in this work).

In addition to the three image-related inputs (Eqs. (2)–(4)), we also consider the time-lagged DNI and DIF measurements (ranging from 0 to 20 min in steps of 5 min) as inputs because: 1) Latest measured DNI are highly informative for intra-hour forecasts of DNI [27] 2) Significant variations of DIF usually associate with cloud enhancement. Cloud enhancement happens when clouds are close to the solar disk and therefore is a indicator of possible ramp events in future [42,43]. Consequently, we consider DIF measurements as inputs to improve the forecast accuracy for ramp events. To make the performance of forecasts comparable, both Bootstrap-ANN model and Hybrid model use the same set of inputs.

3.2. Artificial neural networks

ANNs are widely used for solar modeling and forecasting as classification and regression tools [44–48]. In this work, we employ multilayer preceptron neural network, which is one of the most established ANN architectures which are capable of performing arbitrary non-linear mappings [1,49]. Neurons (the basic processing elements of ANN) are placed in layers. The layers between the first input layer and the last output layer are hidden layers [50]. For short term solar forecasts using cloud information as inputs, the number of hidden layer is set to 1 and the number of neurons per hidden layer is set to 7 as suggested in Ref. [26]. On a hidden layer, each neuron sums the weighted outputs from the previous layer and adds a bias to the sum. Then the sum is processed by an activation function (sigmoidal functions in this work) to generate outputs, which are used as the inputs for neurons on the following layer. The mathematics expression for the signal processing of neurons is

$$Y_i = f\left(\sum_{j=1}^{N}(w_{ij}X_j + \beta_{ij})\right), \tag{5}$$

where Y_i is the output of the i-th neuron on current layer, $f(\cdot)$ is the activation function, w_{ij} and β_{ij} are the weight and bias of the j-th input on the i-th neuron, and X_j is j-th output from previous layer. The weight w_{ij} and bias β_{ij} are determined through a supervised learning process using the training set. In this work, the learning process is the Bayesian regularization process with Levenberg–Marquardt optimization. Once the learning process is finished, the ANN model is able to generate predictions using new inputs.

3.3. Support vector machines

SVM is a useful tool for pattern recognition and data classification [51–55] and has been employed in the field of renewable modeling and forecasting [56–58]. In this work, we use the LIBSVM toolbox provided by Ref. [55]. SVM first maps the input vector x to a feature space where the input vector is associated with a class label (target) $y \in \{01\}$ (0 for lv and 1 for hv). In this work, the SVM uses the same input set as discussed in Section 3.1, and these inputs are linearly scaled. Because the number of the input features is greater than 10, the SVM applied in this work uses linear kernel function as suggested in Ref. [55]. A hyperplane is used by SVM to separate these two classes of vectors:

$$f(x) = w \cdot x + b, \tag{6}$$

where w is a vector normal to the hyperplane and b is a bias term. Optimal hyperplane is identified using a cost function that 1) minimize the misclassification cases and 2) maximize the margin between closest training samples (support vectors) and the hyperplane:

$$F(w, \varepsilon) = \frac{1}{2}\|w\|^2 + C\sum_{i=1}^{N} \varepsilon_i, \tag{7}$$

where C determines the penalty assigned to ε. ε represents misclassification cases. Minimization of Eq. (7) is subject to two constraints:

$$\begin{cases} y_i(w \cdot x_i + b) \geq 1 - \varepsilon_i, & i = 1, 2, \ldots, N \\ \varepsilon_i \geq 0, & i = 1, 2, \ldots N \end{cases}. \tag{8}$$

3.4. Persistence model

The persistence model is the simplest forecast model and is selected as a reference model. The persistence forecast assumes that the clear-sky index remains constant within the forecast horizon. Persistence over clear sky index removes the effect of the diurnal solar variation and achieves high accuracy in periods of low DNI variability. The mathematic expression of the persistence forecast is

$$\widehat{B}_{\mathrm{p}}(t + FH) = \frac{B(t)}{B_{\mathrm{clr}}(t)} \times B_{\mathrm{clr}}(t + FH), \tag{9}$$

where $\widehat{B}_{\mathrm{p}}$ is the persistent prediction, subscript p represents persistence, t is the time point, FH is the forecast horizon, B is the measured DNI values, and B_{clr} is the predicted clear sky DNI from a clear sky model. In this work, we use a empirical clear-sky model

[3,27]. This model computes clear-sky DNI using a seven-order polynomial expression that depends on the sine of the solar elevation angle. The parameters of this polynomial expression are obtained using least square method for 30 clear-sky days selected from the training set. This clear-sky model have advantages in terms of accuracy, simplicity, and ease of implementation when compared with most clear-sky models in literature works [27].

The uncertainty associated with the persistence forecast is estimated using the most recent forecasting errors:

$$\sigma_p(t+FH)^2 = \frac{1}{M}\sum_{i=0}^{M}\left(\widehat{B}_p(t-i\Delta t) - B(t-i\Delta t)\right)^2, \quad (10)$$

where Δt is the forecast interval and M represents the number of forecast instances in the considered lagged period, which is set to 1 h empirically. The errors of the forecast are assumed to be Gaussian distributed [29,30]. Therefore, the persistence PIs with a confidence level of $(1-a)$ are generated using the critical value $z_{1-0.5a}$ of standard normal distribution:

$$\widehat{B}_p(t) \pm z_{1-0.5a}\sigma_p(t). \quad (11)$$

3.5. Bootstrap-ANN model

The Bootstrap method is simple, easy to implement, and therefore is frequently used to generate PIs for ANN point forecasts [29,30,59,60]. This method first randomly samples the training set with replacement to obtain N bootstrap re-sampled sets (N is set to 200 as suggested in Ref. [29]). Then each of these N re-sampled sets is used to train a bootstrap ANN, so N bootstrap ANNs are prepared. With new inputs, predictions from all bootstrap ANNs are used to generate an ensemble prediction:

$$\widehat{B}_f(t) = (1/N)\sum_{i=1}^{N}\widehat{B}_i(t), \quad (12)$$

where subscript f represents true regression in Eq. (1). $\widehat{B}_f$ is the estimation of the true regression term, and the variance of the N bootstrap predictions

$$\sigma_f^2(t) = 1/N\sum_{i=1}^{N}\left(\widehat{B}_i(t) - \widehat{B}_f(t)\right)^2 \quad (13)$$

is used to estimate the uncertainty of the true regression. The magnitude of the variance squared residuals (r) at time t can then be calculated as:

$$r^2(t) = max\left(\left(B(t) - \widehat{B}_f(t)\right)^2 - \sigma_f^2(t), 0\right). \quad (14)$$

Using the same training data, a new ANN is trained to model the white noise σ_e by maximizing the log-likelihood of observed residuals r on the training set that contains M training instances:

$$\sigma_e = argmax_{\sigma_e}\sum_{i-1}^{M} log\left(\frac{1}{\sqrt{2\pi\sigma_e^2(t_i)}}exp\left(-\frac{r^2(t_i)}{2\sigma_e^2(t_i)}\right)\right), \quad (15)$$

where the subscript e represent the white noise in Eq. (1). The final Bootstrap-ANN forecast $\widehat{B}_B$ and associated uncertainty σ_B is calculated using Bayesian estimation:

Table 1
Confusion matrix of classification of DNI variability level.

Classified	Measured	
	lv	hv
lv	True positive (TP)	False positive (FP)
hv	False negative (FN)	True negative (TN)

$$p\left(\widehat{B}_B(t)\middle|\sigma_B(t)\right) = \int p\left(\widehat{B}(t)\middle|\sigma_e(t)\right)p\left(\widehat{B}_f(t)\middle|\sigma_f(t)\right)d\left(\widehat{B}_f(t)\right). \quad (16)$$

With the assumption that errors are Gaussian distributed [30], the posterior prediction $\widehat{B}_B = \widehat{B}_f$ and the total variance $\sigma_B^2(t) = \sigma_f^2(t) + \sigma_e^2(t)$. As a result, the PIs are generated using the critical value $z_{1-0.5a}$:

$$\widehat{B}_B(t) \pm z_{1-0.5a}\sigma_B(t). \quad (17)$$

The Bootstrap-ANN model consists of 201 ANNs: 200 for predicting $\widehat{B}_f$ and 1 for predicting σ_e. As a result, computational cost is one of the main drawbacks for the Bootstrap-ANN model [60]. Therefore, we only employ and test this model as a reference model on the validation set that is based on historical data. Bootstrap-ANN model is not deployed for real-time forecasting.

3.6. The hybrid model

DNI time series and sky images can be categorized into two distinct phases [26,27]: the low DNI variability period (lv), defined as $(B(t+FH) - B(t))/B_{clr}(t) < 0.05$; and the high DNI variability period (hv), defined as $(B(t+FH) - B(t))/B_{clr}(t) \geq 0.05$ lv is usually associated with clear or overcast sky conditions and hv is usually associated with partly cloudy sky conditions.

The training set can be labeled and divided into a lv subset and a hv subset, and two ANN schemes (ANN_{lv} and ANN_{hv}) are trained using the lv subset and the hv subset, respectively. To reduce the computational cost and to simplify the Hybrid model for real time forecasting, both ANN_{lv} and ANN_{hv} are trained to directly predict the Hybrid forecast $\widehat{B}_H(t)$ and associated total uncertainty $\sigma_H(t)$ without considering the uncertainty of the true regression (discussed in Section 3.5). Each of the two ANN schemes needs only 2 ANNs: 1 for predicting $\widehat{B}_H$ and 1 for predicting σ_H. The ANN for modeling $\sigma_H(t)$ is trained using the same maximum likelihood estimation method discussed in Eq. (15) by maximizing the log-likelihood of Hybrid forecast residuals $r_H^2(t_i) = (\widehat{B}_H(t_i) - B(t_i))^2$.

For the proposed Hybrid model, a SVM is first trained using the whole training set to perform the classification of the DNI variability level (0 for lv and 1 for hv). We define a reference persistence classifier to benchmark the performance of the SVM classifier. This persistence classifier assumes the DNI variability level remains the same within the forecast horizon. The trained SVM and two ANN schemes are used to create the Hybrid model, which is defined as:

Table 2
Classification accuracy of DNI variability level on the validation set.

	5-min	10-min	15-min	20-min
Persistence overall	0.84	0.83	0.82	0.81
Persistence for lv	0.89	0.88	0.87	0.86
Persistence for hv	0.71	0.70	0.69	0.66
SVM overall	0.87	0.86	0.86	0.85
SVM for lv	0.87	0.86	0.86	0.85
SVM for hv	0.88	0.87	0.86	0.85

Table 3
Deterministic point forecast results on the validation set in terms of statistical metrics. Boldface font identifies the best performance. MBE, MAE, and RMSE are in (Wm^{-2}).

		5-min	10-min	15-min	20-min
Persistence	MBE	0.6	1.4	2.2	3
	MAE	50.3	64.6	72.1	78.4
	RMSE	128	152.6	164.3	172.5
	s	0.0%	0.0%	0.0%	0.0%
Bootstrap-ANN	MBE	−4.5	−5.1	−4.6	−3.9
	MAE	49.8	60.8	68.5	75.2
	RMSE	111.8	128.9	140.6	150.0
	s	**12.7%**	15.5%	14.4%	**13.1%**
Hybrid	MBE	−3.4	−6.5	−5.9	−5.4
	MAE	47.5	61.5	67.3	72.8
	RMSE	112.6	128.6	138.9	150.7
	s	12.0%	**15.7%**	**15.5%**	12.6%

$$\left\{\widehat{B}(t+FH), \sigma_{\mathrm{H}}(t+FH)\right\} = \begin{cases} \mathrm{ANN}_{\mathrm{lv}}(t) & \text{if} \quad \mathrm{SVM}(t) = 0(\mathrm{lv}) \\ \mathrm{ANN}_{\mathrm{hv}}(t) & \text{if} \quad \mathrm{SVM}(t) = 1(\mathrm{hv}) \end{cases} \tag{18}$$

where the SVM determines which ANN scheme to apply: when the SVM output is 0 (lv), it applies $\mathrm{ANN}_{\mathrm{lv}}$, otherwise it applies $\mathrm{ANN}_{\mathrm{hv}}$. The selected ANN scheme predicts a Hybrid point forecast $\widehat{B}_{\mathrm{H}}(t)$ and a Hybrid forecast variance $\sigma_{\mathrm{H}}(t)$, and the Hybrid PIs are generated as:

$$\widehat{B}_{\mathrm{H}}(t) \pm z_{1-0.5a}\sigma_{\mathrm{H}}(t). \tag{19}$$

The Hybrid model consists of 4 ANNs and 1 SVM in total. Therefore, the computational cost of the Hybrid model is substantially lower than the Bootstrap-ANN model and meets the computation time requirement for real-time applications.

3.7. Assessment metrics

We assess the classifications of the DNI variability level (lv or hv) from persistence classifier and SVM classifier using the confusion matrix shown in Table 1.

The accuracy of classification is defined as the percentage of time points that are classified correctly:

$$\mathrm{Accuracy} = \frac{\mathrm{TP}+\mathrm{TN}}{\mathrm{TP}+\mathrm{TN}+\mathrm{FP}+\mathrm{FN}}; \tag{20}$$

We use four statistical metrics to assess the deterministic predictions of persistence model, Bootstrap-ANN model and Hybrid model: mean biased error (MBE)

Table 5
Results of CWCs for overall, lv, and hv periods on validation set. Boldface font identifies the best performance.

	Models	5-min	10-min	15-min	20-min
Overall	Persistence	6.565	18.892	40.966	86.632
	Bootstrap-ANN	2.392	13.252	21.775	54.389
	Hybrid	**0.242**	**0.274**	**0.282**	**0.293**
lv	Persistence	0.470	0.524	2.542	10.558
	Bootstrap-ANN	0.266	0.686	2.430	9.234
	Hybrid	**0.121**	**0.144**	**0.150**	**0.157**
hv	Persistence	393.515	660.922	955.924	1118.812
	Bootstrap-ANN	350.488	584.006	407.535	398.438
	Hybrid	**0.554**	**8.733**	**5.532**	**4.626**

$$\mathrm{MBE} = \frac{1}{n}\sum_{t=1}^{n}\left(\widehat{B}(t) - B(t)\right), \tag{21}$$

mean absolute error (MAE)

$$\mathrm{MAE} = \frac{1}{n}\sum_{t=1}^{n}\left(\left|\widehat{B}(t) - B(t)\right|\right), \tag{22}$$

root mean square error (RMSE)

$$\mathrm{RMSE} = \sqrt{\frac{1}{n}\sum_{t=1}^{n}\left(\widehat{B}(t) - B(t)\right)^2}, \tag{23}$$

and forecasting skill (s), which measures the improvement of the proposed forecast model (the Bootstrap-ANN or the Hybrid) over the persistence model in terms of RMSE

$$\mathrm{s} = 1 - \frac{\mathrm{RMSE}}{\mathrm{RMSE_p}}. \tag{24}$$

We also use three performance metrics [30,61] to quantitatively assess the PIs:

Prediction interval coverage probability (PICP), which measures whether the target values are covered by the PIs:

$$\mathrm{PICP} = \frac{1}{n}\sum_{i=1}^{n} c_i, \tag{25}$$

where $c_i = 1$ indicates measured DNI value is within the PIs, otherwise $c_i = 0$.

Prediction interval normalized averaged width (PINAW), which measures the informativeness of PIs:

Table 4
Overall PICPs and PINAWs of persistence, Bootstrap-ANN, and Hybrid models for different confidence levels (1-a) on the validation set.

Model	PICP			PINAW					
	1-a	5-min	10-min	15-min	20-min	5-min	10-min	15-min	20-min
Persistence	0.68	0.73	0.70	0.68	0.66	0.132	0.157	0.169	0.178
	0.80	0.78	0.76	0.74	0.73	0.164	0.193	0.208	0.218
	0.90	0.83	0.81	0.80	0.78	0.203	0.238	0.255	0.267
	0.95	0.86	0.85	0.84	0.82	0.233	0.270	0.289	0.302
Bootstrap-ANN	0.68	0.69	0.66	0.64	0.61	0.129	0.149	0.164	0.175
	0.80	0.77	0.74	0.73	0.70	0.161	0.185	0.202	0.215
	0.90	0.85	0.82	0.81	0.79	0.199	0.227	0.247	0.262
	0.95	0.90	0.87	0.86	0.85	0.228	0.258	0.280	0.296
Hybrid	0.68	0.83	0.79	0.79	0.78	0.165	0.188	0.194	0.203
	0.80	0.89	0.87	0.86	0.85	0.202	0.229	0.236	0.246
	0.90	0.93	0.92	0.91	0.90	0.242	0.274	0.282	0.293
	0.95	0.94	0.94	0.93	0.93	0.271	0.306	0.314	0.325

$$\mathrm{PINAW} = \frac{1}{n}\sum_{i=1}^{n}\frac{W_i}{B_{\mathrm{clr}}}, \tag{26}$$

where W_i is the width between the upper and lower bounds of PIs.

Coverage width-based criterion (CWC), which assesses the quality of PIs combining PICP and PINAW:

$$\mathrm{CWC} = \mathrm{PINAW}\left(1 + \gamma(\mathrm{PICP})e^{\eta(1-a-\mathrm{PICP})}\right), \tag{27}$$

where γ depends on the value of PICP:

$$\gamma = \begin{cases} 0 & \mathrm{PICP} \geq 1-a \\ 1 & \mathrm{PICP} < 1-a \end{cases} \tag{28}$$

$1-a$ is the nominal confidence level, η is a parameter that controls the weight of PICP in determining the value of CWC. Coverage probability (PICP) is the most important characteristic of PIs, and invalid PIs should be highly penalized [30]. Therefore, η is set to 50 as suggested in Ref. [30].

4. Results and discussion

4.1. Classification of DNI variability level

The classification performance of the persistence and SVM classifiers on the validation set are listed in Table 2. The persistence classifier slightly outperforms the SVM classifier during lv period. However, the classification accuracy of persistence classifier is substantially lower during hv periods because it is unable to forecast the occurrence of ramps caused by cloud movements [26,27].

The SVM classifier achieves higher overall accuracy for forecast horizons from 5 min to 20 min. The classification accuracy of SVM classifier exceeds 85% for both lv and hv periods. Through analysis, we find that the misclassifications of SVM classifier are usually caused by two reasons: 1) Because of the image glare, Pixels in circumsolar region of sky images have high magnitude of RBR that are close or overlap cloudy RBR. 2) The clear sky model is less accurate in modeling the DNI in low sun elevation period [27]. Therefore, the algorithm occasionally identifies the discrepancy between measured and modeled clear-sky DNI as pseudo-ramps. The above two reasons impair the quality of the inputs and targets to the classifier, adversely affect the training process of classifier, and degenerate the accuracy of SVM classifier.

4.2. Deterministic point forecasts

The persistence model, Bootstrap-ANN model, and the Hybrid model are evaluated on the validation set and the results of point forecasts are presented in Table 3 in terms of statistic metrics. All three models show small bias. In terms of RMSE and s, both Bootstrap-ANN and Hybrid models significantly outperform the persistence model achieving 12%–16% improvements depending on the forecast horizon. The forecast skills of the Hybrid model are not significantly higher than the Bootstrap-ANN model mainly because of the misclassifications of SVM. When SVM misclassification occurs, the Hybrid model applies the inappropriate ANN scheme resulting in a point prediction with relatively higher errors, especially during the hv periods. Nevertheless, with the SVM classifier that achieves an accuracy above 85% for hv period, the PIs generated by the Hybrid model are superior to PIs generated by the Bootstrap-ANN during hv period (will be discussed in Section 4.3).

4.3. Validation of prediction intervals

Prediction intervals are generated from persistence, Bootstrap-ANN and Hybrid models for four nominal confidence levels (68.3%, 80%, 90%, and 95%) and are assessed on the validation set. The validation results are presented in Tables 4 and 5. Ideally, PIs should have high PICP and low PINAW indicating high coverage probability of target values and high informativeness, respectively. At the same confidence level, the PIs generated by the Hybrid model mostly have higher PICPs and PINAWs than the PIs generated by the persistence and Bootstrap-ANN models (shown in Table 4). The results of Table 4 are illustrated in a 2-D plot (Fig. 2) where x-axis and y-axis represent PICP and PINAW, respectively. In Fig. 2, at the same level of PINAW, the PIs of the Hybrid model have significantly higher PICPs than the other two models. Therefore, in Fig. 2, Hybrid markers achieve lower ratios of PINAW/PICP than persistence and Bootstrap-ANN markers.

PIs are considered as valid if their PICPs are greater than their nominal confidence level [30]. For instance, Hybrid PIs using 90% nominal confidence interval achieve a PICP of 92.8% for 5-min forecast on the validation set and therefore are considered as valid PIs. As shown in Table 4, the Hybrid model is the only model that achieves PICPs mostly greater than their nominal confidence levels. PICPs of persistence and Bootstrap-ANN models are usually lower than their nominal confidence levels.

Consequently, CWCs of the Hybrid model are substantially lower than the CWCs of the other two models for various forecast horizons (shown in Table 5). In addition, the CWCs of both persistence and Bootstrap-ANN models increase tremendously for hv period. This increase in CWCs due to the decrease of PICPs during cloudy weather is also observed in Ref. [30]. The Hybrid model, which applies specific forecasting scheme for different DNI variability levels, consistently achieves CWCs < 10 for both lv and hv periods.

4.4. Real time forecasting

We monitor and analyze the persistence and the Hybrid forecasts in real time during the period from August 1, 2014 to November 23, 2014. The processing time to operate the forecasts for each time point is less than 5 s. PIs are generated using a nominal confidence level of 90%.

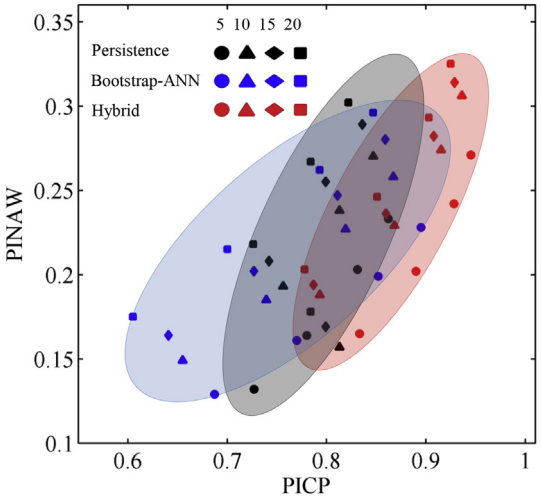

Fig. 2. Forecast results of persistence, Bootstrap-ANN, and Hybrid models for various forecast horizons and confidence levels in 2-D map. X-axis represents PICP, y-axis represents PINAW. Each marker stands for one validation result.

Table 6
Classification accuracy of DNI variability level in real time forecasting.

	5-min	10-min	15-min	20-min
Persistence overall	0.89	0.87	0.86	0.85
Persistence for lv	0.92	0.91	0.91	0.91
Persistence for hv	0.78	0.68	0.64	0.60
SVM overall	0.91	0.87	0.87	0.86
SVM for lv	0.92	0.89	0.89	0.89
SVM for hv	0.86	0.85	0.83	0.82

The classification accuracy of persistence and SVM classifiers are presented in Table 6, and the statistical results for the deterministic point forecasts are presented in Table 7. Hybrid point forecasts significantly outperform the reference persistence model and achieve forecast skills between 10% and 13% depends on forecast horizons. Comparing to the validation set presented in the previous section, the operational period for real-time forecasts has higher fraction of clear (lv) time. Therefore, both persistence and Hybrid model achieve lower MAE and RMSE in real-time than those on the validation set (shown in Fig. 2 and Table 5).

The results for PIs are presented in Table 8. PIs are considered as invalid if their PICPs are less than their nominal confidence level ([30]). In the real-time scenario, the Hybrid model achieves positive margins between PICPs and corresponding nominal confidence levels for both hv and lv periods. Therefore, the PIs of the Hybrid model are valid and reliable regardless of the variability level of DNI. The Hybrid PIs are highly informative for lv periods and achieve low magnitudes of PINAWs. For hv period, the PINAWs of Hybrid PIs are large because of the highly variable nature of DNI.

Comparing to persistence PIs whose PICPs decrease when forecast horizon increases, Hybrid PIs of different forecast horizons (5-, 10-, 15- and 20-min) achieves similar levels of PICP. The PINAW of both forecasts for longer horizons are larger than their counterparts for shorter horizons. As we observed in Table 3, Hybrid deterministic point forecasts of longer horizons have larger errors than that of shorter horizons. Therefore, the forecast models of longer horizons are trained using larger forecast residuals (r_H^2) and tend to predict larger uncertainty term (σ_H) and to generate PIs of broader widths. The increase of uncertainties with respect to the increase of forecast horizons is also observed in Ref. [30]. With a relatively lower level of informativeness (overall <8% higher in PINAW), the PIs of longer horizons achieve similar PICPs as the PIs of shorter horizons.

Representative time series of 10-min horizon forecasts are plotted in Fig. 3. During the lv periods (shown in Fig. 3a and b), the PIs of both the persistence model and the Hybrid model achieve excellent coverage probability with high levels of informativeness. During the hv periods (shown in Fig. 3c and d), the Hybrid PIs covers most of the target values achieving significantly higher PICPs than PIs from the persistence model. The PIs generated by the persistence have low PICPs because their predictions of ramp events are usually subsequent in time to the true ramp events.

Sample time-series of the Hybrid PIs and corresponding measured DNI for all forecast horizons (5, 10, 15 and 20 min) are shown in Fig. 4. Persistence PIs are presented for comparison. When the forecast horizon increases, the lagging of persistence PIs increases and the corresponding coverage probability gradually decreases. The Hybrid PIs of different forecast horizons achieve similar levels of coverage probability. However, the average widths of Hybrid PIs for longer horizons are wider than their counterparts for shorter horizons. As we observed in Table 7, Hybrid deterministic point forecasts of longer horizons are characterized by larger RMSEs. Therefore, the forecasts for longer horizons tend to have

Table 7
Results for real-time point forecasts in terms of statistical metrics. MBE, MAE, and RMSE are in (Wm^{-2}).

		5-min	10-min	15-min	20-min
Persistence	MBE	−0.4	−1.2	−2.2	−3.4
	MAE	37.5	45.8	53.4	58.6
	RMSE	102.6	124.3	139.0	149.1
	s	0.0%	0.0%	0.0%	0.0%
Hybrid	MBE	1.2	2.11	4.0	5.3
	MAE	35.7	44.2	51.8	56.8
	RMSE	93.1	111.5	122.3	131.8
	s	10.0%	10.3%	12.2%	11.6%

Table 8
Real time results of PICPs, PINAWs, and CWCs for overall, lv, and hv periods.

			5-min	10-min	15-min	20-min
Overall	PICP	Persistence	0.90	0.86	0.83	0.80
		Hybrid	0.97	0.95	0.96	0.95
	PINAW	Persistence	0.14	0.17	0.18	0.19
		Hybrid	0.22	0.24	0.28	0.30
	CWC	Persistence	0.32	1.25	6.90	32.27
		Hybrid	0.22	0.24	0.28	0.30
lv	PICP	Persistence	0.94	0.90	0.86	0.83
		Hybrid	0.98	0.97	0.98	0.98
	PINAW	Persistence	0.06	0.08	0.08	0.09
		Hybrid	0.11	0.11	0.13	0.15
	CWC	Persistence	0.06	0.08	0.57	3.09
		Hybrid	0.11	0.11	0.15	0.17
hv	PICP	Persistence	0.75	0.71	0.71	0.72
		Hybrid	0.92	0.92	0.92	0.91
	PINAW	Persistence	0.51	0.58	0.61	0.62
		Hybrid	0.61	0.71	0.72	0.73
	CWC	Persistence	75.02	779.91	816.41	547.37
		Hybrid	0.61	0.71	0.72	0.73

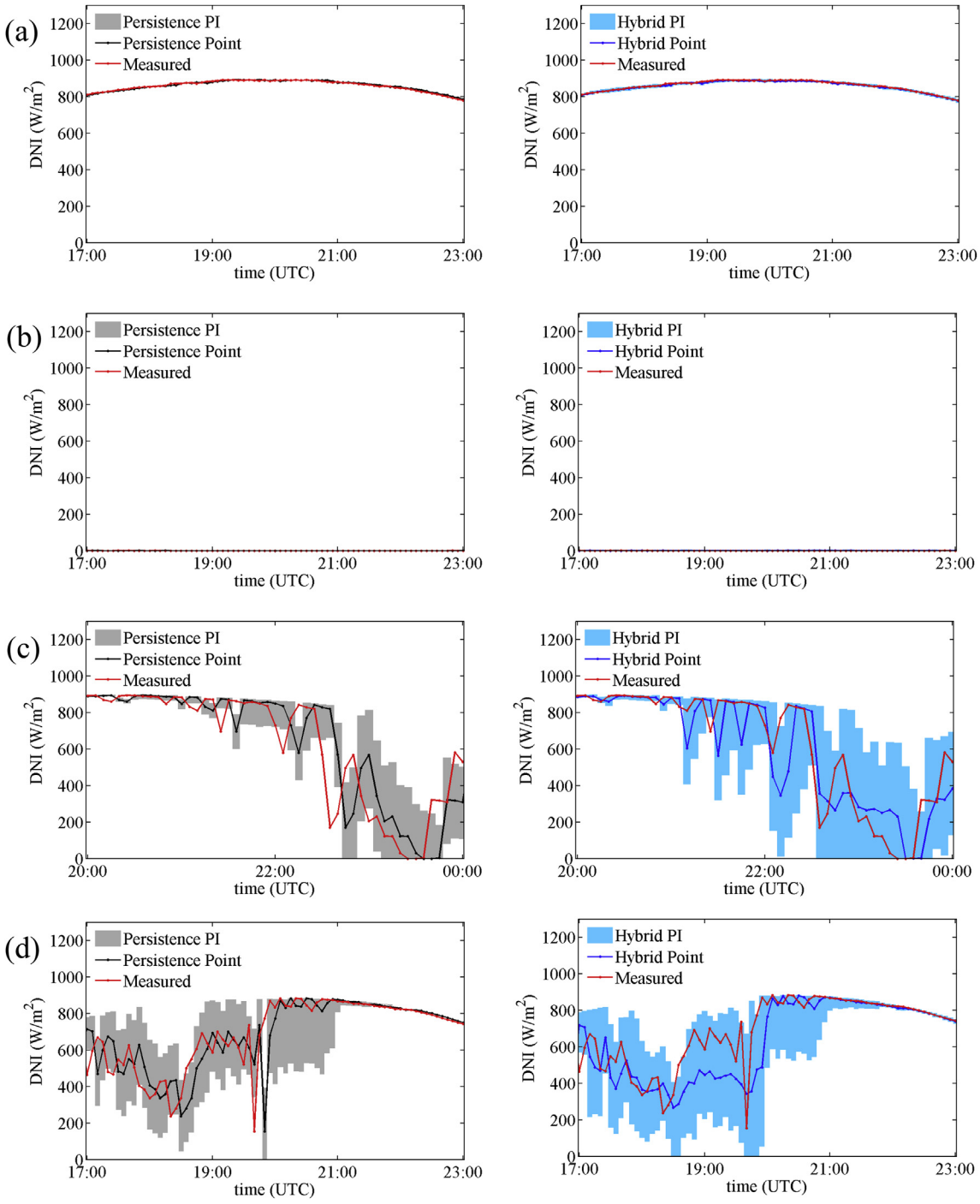

Fig. 3. Sample time series of 10-min horizon forecasts from the persistence and the Hybrid models: (a) clear period (2014-10-19), (b) overcast period (2014-11-13), (c) partly cloudy period 1 (2014-10-10), and (d) partly cloudy period 2 (2014-11-04).

larger residual (r_H^2) and larger uncertainty term (σ_H) resulting in wider PIs. The increase of uncertainty with respect to the increase of forecast horizon is also observed in Ref. [30]. Wider PIs for longer horizons achieve similar PICPs but higher PINAWs than the PIs for shorter horizons.

The PIs of the Hybrid model achieve high coverage probability during ramp events regardless of weather and forecast horizon. Accurate forecast of irradiance ramps is essential to solar power plants for inverter control, plant management and real-time dispatch operations [62,63]. The Hybrid PIs provide possible ranges for the DNI ramps, quantify the uncertainty in the point predictions, and therefore provide useful information for plants or grid operators to make informed decisions to mitigate the weather-dependent variance of solar power production.

5. Conclusions

A Hybrid multilayered computational model is developed to generate prediction intervals (PIs) for intra-hour forecast of DNI.

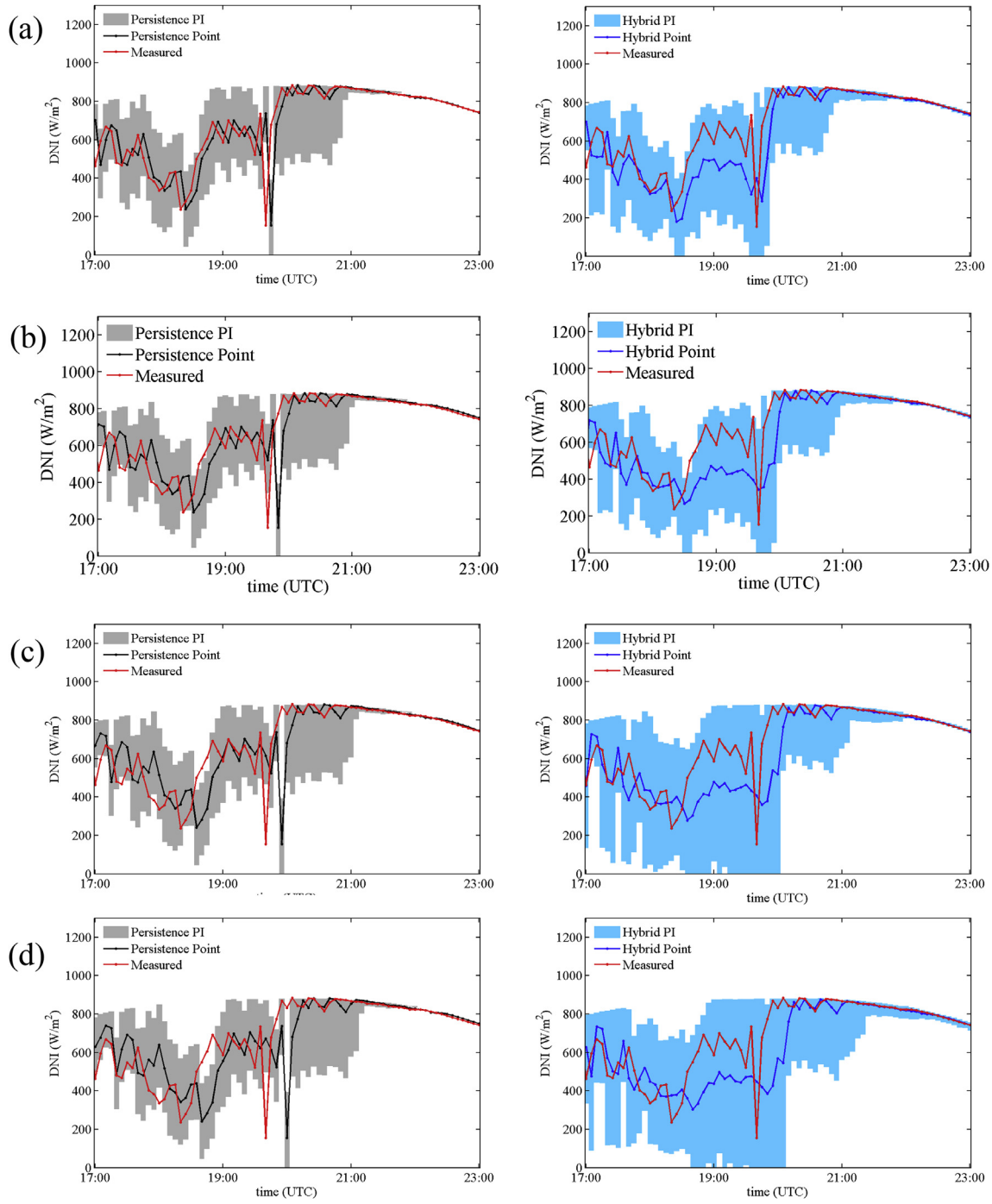

Fig. 4. Sample time series of different horizon forecasts from the persistence model (left column) and the Hybrid model (right column) for partly cloudy period 2 (2014-11-04): (a) 5-min, (b) 10-min, (c) 15-min, and (d) 20-min.

The proposed Hybrid model integrates Support Vector Machine (SVM) classifiers, Artificial Neural Network (ANN) algorithms, and sky-imaging techniques. We train the multilayered model using 12-month of irradiance and sky-imaging data collected at our solar meteorology station in Folsom, California. The forecasting model first uses a SVM classifier to categorize the current time into either low DNI variability period (lv) or high DNI variability period (hv). Then based on the present DNI variability level, the Hybrid model adaptively applies specific ANN schemes to generate PIs for 5-, 10-, 15-, and 20-min forecast horizons. Persistence and Bootstrap-ANN models are employed as the reference models to benchmark the performance of the proposed Hybrid model. The PIs generated from the three models are validated for six months of validation data and quantitatively assessed in terms of three metrics: PI coverage probability (PICP), PI normalized average width (PINAW), and coverage width-based criterion (CWC). The Hybrid model is operational in real time at the same observatory in Folsom since July 1st, 2014.

The results for both the model validation phase and the continuous operational forecasts show that:

1. At similar level of PINAW, the Hybrid PIs substantially outperform the reference models in term of PICP and CWC regardless of the forecast horizon and the level of DNI variability.
2. The Hybrid PIs successfully quantify the uncertainty of deterministic point predictions, provide possible range for target DNIs, and achieve coverage probabilities which are substantially better than the nominal confidence levels.
3. The Hybrid PIs respond rapidly to the changes of DNI variability level and achieve high coverage probability during ramp events.

The proposed Hybrid model thus provide highly relevant information to mitigate the effects of weather-dependent variability on solar power generation.

Acknowledgments

Prof. Coimbra and Dr. Pedro are partially funded by the National Science Foundation (NSF) EECS-EPAS award No. 1201986, which is managed by Dr. Paul Werbos. Ms. B. Wang from U.C. San Diego assisted in the analysis of Section 3.

References

[1] Inman R, Pedro H, Coimbra CFM. Solar forecasting methods for renewable energy integration. Prog Energy Combust Sci 2013;39(6):535–76.
[2] Singh GK. Solar power generation by PV (photovoltaic) technology: a review. Energy 2013;53:1–13.
[3] Quesada-Ruiz S, Chu Y, Tovar-Pescador J, Pedro HTC, Coimbra CFM. Cloud-tracking methodology for intra-hour DNI forecasting. Sol Energy 2014;102:267–75.
[4] Chu Y, Urquhart B, Gohari SMI, Pedro HTC, Kleissl J, Coimbra CFM. Short-term reforecasting of power output from a 48 MWe solar PV plant. Sol Energy 2015a;112:68–77.
[5] Yap WK, Karri V. An off-grid hybrid PV/diesel model as a planning and design tool, incorporating dynamic and ANN modelling techniques. Renew Energy 2015;78(0):42–50.
[6] Elizondo D, Hoogenboom G, McClendon RW. Development of a neural network model to predict daily solar radiation. Agric For Meteorol 1994;71(1):115–32.
[7] Sfetsos A, Coonick AH. Univariate and multivariate forecasting of hourly solar radiation with artificial intelligence techniques. Sol Energy 2000;68(2):169–78.
[8] Santos JM, Pinazo JM, Canada J. Methodology for generating daily clearness index index values K_t starting from the monthly average daily value $\overline{K}_t$. Determining the daily sequence using stochastic models. Renew Energy 2003;28(10):1523–44.
[9] Sinha S, Kumar S, Matsumoto T, Kojima T. Application of system identification modeling to solar hybrid systems for predicting radiation, temperature and load. Renew Energy 2001;22(1–3):281–6.
[10] Chaabene M, Ben Ammar M. Neuro-fuzzy dynamic model with Kalman filter to forecast irradiance and temperature for solar energy systems. Renew Energy 2008;33(7):1435–43.
[11] Cao J, Lin X. Study of hourly and daily solar irradiation forecast using diagonal recurrent wavelet neural networks. Energy Convers Manag 2008;49(6):1396–406.
[12] Lave M, Kleissl J. Solar variability of four sites across the state of Colorado. Renew Energy 2010;35(12):2867–73.
[13] Martín L, Zarzalejo LF, Polo J, Navarro A, Marchante R, Cony M. Prediction of global solar irradiance based on time series analysis: application to solar thermal power plants energy production planning. Sol Energy 2010;84(10):1772–81.
[14] Mellit A, Pavan AM. A 24-h forecast of solar irradiance using artificial neural network: application for performance prediction of a grid-connected PV plant at Trieste, Italy. Sol Energy 2010;84(5):807–21.
[15] Mellit A, Eleuch H, Benghanem M, Elaoun C, Pavan AM. An adaptive model for predicting of global, direct and diffuse hourly solar irradiance. Energy Convers Manag 2010;51(4):771–82.
[16] Pedro HTC, Coimbra CFM. Assessment of forecasting techniques for solar power production with no exogenous inputs. Sol Energy 2012;86(7):2017–28.
[17] Marquez R, Coimbra CFM. Proposed metric for evaluation of solar forecasting models. ASME J Sol Energy Eng 2013a;135:0110161–9.
[18] Marquez R, Gueorguiev VG, Coimbra CFM. Forecasting of global horizontal irradiance using sky cover indices. ASME J Sol Energy Eng 2013a;135:0110171–5.
[19] Marquez R, Pedro HTC, Coimbra CFM. Hybrid solar forecasting method uses satellite imaging and ground telemetry as inputs to ANNs. Sol Energy 2013b;92:176–88.
[20] Nonnenmacher L, Kaur A, Coimbra CFM. Verification of the SUNY direct normal irradiance model with ground measurements. Sol Energy 2014;99:246–58.
[21] Hammer A, Heinemann D, Lorenz E, Luckehe B. Short-term forecasting of solar radiation: a statistical approach using satellite data. Sol Energy 1999;67:139–50.
[22] Perez R, Kivalov S, Schlemmer J, Hemker K, Renne D, Hoff TE. Validation of short and medium term operational solar radiation forecasts in the US. Sol Energy 2010;84(5):2161–72.
[23] Chow CW, Urquhart B, Lave M, Dominguez A, Kleissl J, Shields J, et al. Intra-hour forecasting with a total sky imager at the UC San Diego solar energy testbed. Sol Energy 2011;85(11):2881–93.
[24] Marquez R, Coimbra CFM, Intra-Hour DNI. Forecasting methodology based on cloud tracking image analysis. Sol Energy 2013b;91:327–36.
[25] Nonnenmacher L, Coimbra CFM. Streamline-based method for intra-day solar forecasting through remote sensing. Sol Energy 2014;108:447–59.
[26] Chu Y, Pedro HTC, Nonnenmacher L, Inman RH, Liao Z, Coimbra CFM. A smart image-based cloud detection system for intra-hour solar irradiance forecasts. J Atmos Ocean Technol 2014;31:1995–2007.
[27] Chu Y, Pedro HTC, Coimbra CFM. Hybrid intra-hour DNI forecasts with sky image processing enhanced by stochastic learning. Sol Energy 2013;98:592–603.
[28] Chu Y, Pedro HTC, Li M, Coimbra CFM. Real-time forecasting of solar irradiance ramps with smart image processing. Sol Energy 2015;114:91–104.
[29] Carney JG, Cunningham P, Bhagwan U. Confidence and prediction intervals for neural network ensembles. Neural networks, 1999. IJCNN'99. International Joint Conference on, vol. 2. IEEE; 1999. p. 1215–8.
[30] Khosravi A, Nahavandi S, Creighton D. Prediction intervals for short-term wind farm power generation forecasts. Sustain Energy, IEEE Trans 2013;4(3):602–10.
[31] Iversen EB, Morales JM, Møller JK, Madsen H. Probabilistic forecasts of solar irradiance using stochastic differential equations. Environmetrics 2014;25(3):152–64.
[32] Pinson P, Nielsen HA, Møller JK, Madsen H, Kariniotakis GN. Non-parametric probabilistic forecasts of wind power: required properties and evaluation. Wind Energy 2007;10(6):497–516.
[33] Bracale A, Caramia P, Carpinelli G, Di Fazio AR, Ferruzzi G. A Bayesian method for short-term probabilistic forecasting of photovoltaic generation in smart grid operation and control. Energies 2013;6(2):733–47.
[34] Tapakis R, Charalambides AG. Equipment and methodologies for cloud detection and classification: a review. Sol Energy 2013;95(0):392–430.
[35] Li Q, Lu W, Yang J. A hybrid thresholding algorithm for cloud detection on ground-based color images. J Atmos Ocean Technol 2011;28:1286–96.
[36] Souza-Echer MP, Pereira EB, Bins LS, Andrade MAR. A simple method for the assessment of the cloud cover state in high-latitude regions by a ground-based digital camera. J Atmos Ocean Technol 2006;23:437–47.
[37] Long CN, Sabburg JM, Calbó J, Pages D. Retrieving cloud characteristics from ground-based daytime color all-sky images. J Atmos Ocean Technol 2006;23:633–52.
[38] Yang J, Lü W, Ma Y, Yao W, Li Q. An automatic ground based cloud detection method based on adaptive threshold. J Appl Meteorol Sci 2009;20:713–21.
[39] Heinle A, Macke A, Srivastav A. Automatic cloud classification of whole sky images. Atmos Meas Tech 2010;3:557–67.
[40] Neto SLM, von Wangenheim A, Pereira EB, Comunello E. The use of Euclidean geometric distance on RGB color space for the classification of sky and cloud patterns. J Atmos Ocean Technol 2010;27:1504–17.
[41] Ghonima MS, Urquhart B, Chow CW, Shields JE, Cazorla A, Kleissl J. A method for cloud detection and opacity classification based on ground based sky imagery. Atmos Meas Tech Discuss 2012;5:4535–69.
[42] Yordanov GH, Midtgård O, Saetre TO, Nielsen HK, Norum LE. Overirradiance (cloud enhancement) events at high latitudes. IEEE J Photovolt 2013;3(1):271–7.
[43] Luoma J, Kleissl J, Murray K. Optimal inverter sizing considering cloud enhancement. Sol energy 2012;86(1):421–9.
[44] Bishop CM. Neural networks and their applications. Rev Sci Instrum 1994;65(6):1803–32.
[45] Al-Alawi SM, Al-Hinai HA. An ANN-based approach for predicting global radiation in locations with no direct measurement instrumentation. Renew Energy 1998;14:199–204.
[46] Mellit A, Kalogirou SA. Artificial intelligence techniques for photovoltaic applications: a review. Prog Energy Combust Sci 2008;34(5):574–632.
[47] Marquez R, Coimbra CFM. Forecasting of global and direct solar irradiance using stochastic learning methods, ground experiments and the NWS database. Sol Energy 2011;85(5):746–56.
[48] Chen SX, Gooi HB, Wang MQ. Solar radiation forecast based on fuzzy logic and neural networks. Renew Energy 2013;60(0):195–201.
[49] Sözen A, Arcaklıoğlu E, Özalp M, Çağlar N. Forecasting based on neural network approach of solar potential in Turkey. Renew Energy 2005;30(7):1075–90.
[50] Garca-Domingo B, Piliougine M, Elizondo D, Aguilera J. CPV module electric characterisation by artificial neural networks. Renew Energy 2015;78(0):173–81.
[51] Burges CJC. A tutorial on support vector machines for pattern recognition. Data Min Knowl Discov 1998;2(2):121–67.
[52] Vapnik V. The nature of statistical learning theory. New York: Springer; 2000.

[53] Huang C, Davis LS, Townshend JRG. An assessment of support vector machines for land cover classification. Int J Remote Sens 2002;23(4):725–49.
[54] Melgani F, Bruzzone L. Classification of hyperspectral remote sensing images with support vector machines. Geosci Remote Sens IEEE Trans 2004;42(8):1778–90.
[55] Chang C, Lin C. LIBSVM: a library for support vector machines. ACM Trans Intell Syst Technol 2011;2. 27:1–27:27.
[56] Foley AM, Leahy PG, Marvuglia A, McKeogh EJ. Current methods and advances in forecasting of wind power generation. Renew Energy 2012;37(1):1–8.
[57] Zeng J, Qiao W. Short-term solar power prediction using a support vector machine. Renew Energy 2013;52(0):118–27.
[58] Zagouras A, Pedro HTC, Coimbra CFM. On the role of lagged exogenous variables and spatiotemporal correlations in improving the accuracy of solar forecasting methods. Renew Energy 2015;78(0):203–18.
[59] Heskes T. Practical confidence and prediction intervals. Adv Neural Info Process Syst 1997;9:176–82.
[60] Khosravi A, Nahavandi S, Creighton D, Atiya AF. Lower upper bound estimation method for construction of neural network-based prediction intervals. Neural Netw IEEE Trans 2011;22(3):337–46.
[61] Khosravi A, Nahavandi S, Creighton D. Construction of optimal prediction intervals for load forecasting problems. Power Syst IEEE Trans 2010;25(3):1496–503.
[62] Zhang J, Hodge B, Florita A, Lu S, Hamann HF, Banunarayanan V. Metrics for evaluating the accuracy of solar power forecasting. Tech. Rep. National Renewable Energy Laboratory; 2013. NREL/CP-5500–60142
[63] Florita A, Hodge B, Orwig K. Identifying wind and solar ramping events. In: Green technologies conference, 2013 IEEE. IEEE; 2013. p. 147–52.